Hydrothermal Synthesis g-C$_3$N$_4$/Nano-InVO$_4$ Nanocomposites and Enhanced Photocatalytic Activity for Hydrogen Production under Visible Light Irradiation

Bo Hu,[†] Fanpeng Cai,[‡] Tianjun Chen,[†] Mingshan Fan,[†] Chengjie Song,[§] Xu Yan,[†] and Weidong Shi*,[†]

[†]School of Chemistry and Chemical Engineering, Jiangsu University, Xuefu Road 301, Zhenjiang, 212013, P. R. China
[‡]School of Biology and Chemical Engineering, Jiangsu University of Science and Technology, Zhenjiang, 212003, P. R. China
[§]School of Environmental and Safety Engineering, Changzhou University, Changzhou, 213000, P. R. China

S Supporting Information

ABSTRACT: We synthesized g-C$_3$N$_4$/nano-InVO$_4$ heterojunction-type photocatalysts by in situ growth of InVO$_4$ nanoparticles onto the surface of g-C$_3$N$_4$ sheets via a hydrothermal process. The results of SEM and TEM showed that the obtained InVO$_4$ nanoparticles 20 nm in size dispersed uniformly on the surface of g-C$_3$N$_4$ sheets, which revealed that g-C$_3$N$_4$ sheets was probably a promising support for in situ growth of nanosize materials. The achieved intimate interface promoted the charge transfer and inhibited the recombination rate of photogenerated electron–hole pairs, which significantly improved the photocatalytic activity. A possible growth process of g-C$_3$N$_4$/nano-InVO$_4$ nanocomposites was proposed based on different mass fraction of g-C$_3$N$_4$ content. The obtained g-C$_3$N$_4$/nano-InVO$_4$ nanocomposites could achieve effective separation of charge-hole pairs and stronger reducing power, which caused enhanced H$_2$ evolution from water-splitting compared with bare g-C$_3$N$_4$ sheets and g-C$_3$N$_4$/micro-InVO$_4$ composites, respectively. As a result, the g-C$_3$N$_4$/nano-InVO$_4$ nanocomposite with a mass ratio of 80:20 possessed the maximum photocatalytic activity for hydrogen production under visible-light irradiation.

KEYWORDS: g-C$_3$N$_4$, InVO$_4$, nanocomposites, interface, H$_2$ production from water splitting, heterojunction
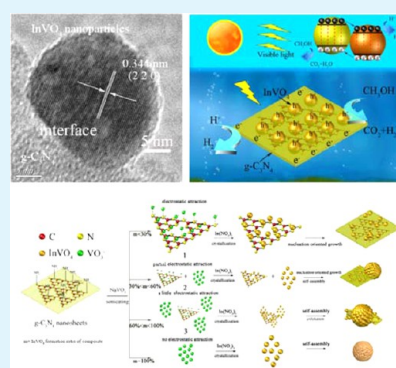
INTRODUCTION

The conversion of solar energy into hydrogen energy is an effective and promising way for solving the energy problem of human society in 21st century. Water splitting for hydrogen production is considered to be a most attractive way to realize this energy conversion.[1−3] Although thousands of inorganic and organic semiconductor photocatalysts have been developed since the 1970s,[4,5] the photocatalyst activity of H$_2$ production for a single-component photocatalyst system is still unsatisfactory.[6,7] In a typical single-component photocatalyst system, the photogenerated electrons and holes of single photocatalyst recombine rapidly before migrating to the surface, which significantly reduces photocatalyst activity. In order to inhibit electron–hole recombination, constructing a heterojunction-type photocatalytic system has been developed, which improves the rate of charge transfer and significantly enhances the photocatalytic activity.[8−11] However, kinetically and thermodynamically, the redox ability of photogenerated electrons and holes after charge transfer is reduced.[12] Therefore, band structure of semiconductor photocatalysts in a typical heterojunction-type photocatalytic system for H$_2$ production should satisfy harsh conditions, such as strong redox ability for H$_2$ production, proper difference of energy level for charge transfer, and narrow band gap for visible-light absorption.

Recently, a novel organic semiconductor photocatalyst graphitic carbon nitride (g-C$_3$N$_4$) has attracted considerable attention.[13,14] Besides, the metal-free photocatalyst possesses many attractive chemical and physical properties, especially a highly negative conduction band level (−1.12 eV) for photocatalytic H$_2$ production.[15,16] However, the high recombination of photogenerated electron–hole pairs reduced its photocatalyst activity of H$_2$ production, which has become a primary problem for the application of g-C$_3$N$_4$.[17] To solve this problem, many effective means were used to increase the rate of electron–hole separation, such as loaded noble nanoparticles,[18] heterojunctions,[19−22] nanomodification,[23] sulfur-doped,[24] and Z-scheme.[25] Among them, constructing a heterojunction-type photocatalytic system has attracted much attention because the typical two-dimensional (2D) sheets of g-C$_3$N$_4$ could provide a suitable scaffold for contacting with other nanosized photocatalysts and achieving nanocomposites with promising interface, which is beneficial to improving the rate of charge transfer.[26,27] In 2011, TiO$_2$-g-C$_3$N$_4$ composites were first synthesized for enhancing the H$_2$ evolution from water-splitting.[28] After that, some investigators have coupled g-C$_3$N$_4$

Scheme 1. Synthesis Process of the g-C$_3$N$_4$/InVO$_4$ Nanocomposites
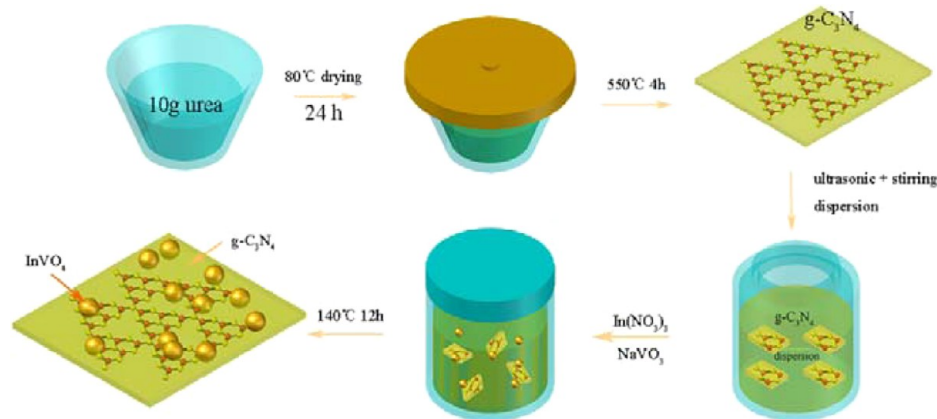
with various UV-response semiconductors, such as TiO$_2$,[29,30] ZnS.[31] However, the phase of UV-light-response photocatalyst can not be excited under visible light irriatation, which will reduce the utilization of solar energy. To overcome the drawbacks, some g-C$_3$N$_4$-based photocatalytic systems consisted of sulfides (CdS,[32,33] MoS$_2$[34]) have been reported. However, as we all know, the poor photocorrosion and self-oxidation of sulfides would significantly reduce the stability.[35] Interestingly, a type of photocatalytic system based on multiple metal oxide and g-C$_3$N$_4$, such as g-C$_3$N$_4$/SrTiO$_3$:Rh,[36] ZnFe$_2$O$_4$/g-C$_3$N$_4$[37] showed excellent and stable photocatalytic activity for H$_2$ production.

InVO$_4$ is a promising photocatalyst for H$_2$ production under visible light irradiation.[38] The conduction band of InVO$_4$ was suitable for H$_2$ production.[39] In addition, many reports indicate that the desired morphology and size of photocatalysts could regulate the position of the energy band for achieving higher redox ability.[40,41] Yan et al. reported that the nanosized InVO$_4$ nanoparticles with the size of 20 nm showed higher photocatalytic activity of H$_2$ production than InVO$_4$ microspheres.[42,43] Consequently, constructing a heterojunction-type photocatalytic system based on g-C$_3$N$_4$ sheets and InVO$_4$ nanoparticles is a feasible and useful process for H$_2$ production.

Herein, we synthesized g-C$_3$N$_4$/nano-InVO$_4$ nanocomposites by introducing g-C$_3$N$_4$ sheets to the InVO$_4$ precursor solution in hydrothermal reaction. The result showed that InVO$_4$ nanoparticles and g-C$_3$N$_4$ sheets were put in contact to achieve desired nanojunctions with an intimate interface, which InVO$_4$ nanoparticles are tightly and uniformly dispersed on the surface of g-C$_3$N$_4$. The functional groups (amino groups) and positive charge on the surface of g-C$_3$N$_4$ sheets probably play a crucial influence on the growth of InVO$_4$ nanoparticles. The photocatalytic activities were investigated by H$_2$ production from methanol aqueous solution. Furthermore, a possible growth process of g-C$_3$N$_4$/nano-InVO$_4$ nanocomposites and a mechanism of enhancing photocatalytic activity were thoroughly studied.

2. EXPERIMENTAL SECTION

2.1. Materials. Urea, sodium metavanadate(NaVO$_3$·2H$_2$O), and Indium nitrate (In(NO$_3$)$_3$·4.5H$_2$O) were purchased from Aladdin (P.R. China). All chemicals were used as received without further purification. Water was obtained from a Hitech-Kflow water purification system (Hitech, P.R. China).

2.2. Preparation of g-C$_3$N$_4$/InVO$_4$ Nanocomposites. Graphitic carbon nitrides (g-C$_3$N$_4$) were synthesized by thermal treatment. First,

10 g of urea was placed in an alumina crucible with a cover. After being dried at 60 °C for 2 days, the urea was heated in a covered crucible to 550 °C in a muffle furnace at a heating rate of 2.3 °C min^{-1}, and then maintained at 550 °C for 4 h.[13] Finally, the obtained products were naturally cooled to room temperature.

The g-C$_3$N$_4$/InVO$_4$ nanocomposites were prepared through a hydrothermal strategy. Typically, 0.2 g of as-prepared g-C$_3$N$_4$ and a certain amount of NaVO$_3$·2H$_2$O were added into a beaker containing 50 mL of pure water and vigorously magnetically stirred for 10 min. In(NO$_3$)$_3$ solution was added slowly to the suspension in a molar ratio of In^{3+}: V^{5+} = 1:1. After stirring for another 30 min, the dispersion was transferred to a 100 mL polytetrafluoroethylene-lined stainless autoclave, and was heated at 140 °C for 12 h and then allowed to cool to room temperature. The solid product was collected by centrifugation, washed thoroughly with water and ethanol, and dried at 60 °C. The process is shown in Scheme 1. For comparison, pure InVO$_4$ was prepared similarly without introducing g-C$_3$N$_4$ sheets to the InVO$_4$ precursor solution. Pure g-C$_3$N$_4$ was prepared similarly without the addition of InVO$_4$. As-prepared composites with expected InVO$_4$ mass fraction of composites, such as 0, 10, 20, 30, 60, 80, and 100% (pure InVO$_4$) are referred to as A0, A10, A20, A30, A60, A80, and A100, respectively.

2.3. Characterization. The products were characterized by X-ray diffraction measurements carried out on X-ray diffractometer (XRD, Bruker D8 Advance diffractometer) with Cu−Kα radiation in the range of 10−80° at a scanning rate of 7°min^{-1}. Scanning electron microscopy (SEM) images were characterized by an S-4800 field emission SEM (FESEM, Hitachi, Japan). F20 S-TWIN electron microscope (Tecnai G2, FEI Co.), using a 200 kV accelerating voltage was used to characterize transmission electron microscopy (TEM) images. The photoluminescence spectra were obtained on a F4500 (Hitachi, Japan) photoluminescence detector. Fourier transform infrared spectroscopy (FTIR) was performed as KBr discs on a Nicolet 6700 spectrometer. A UV−vis spectrophotometer (UV2450, Shimadzu, Japan) was used to characterize UV−vis diffused reflectance spectra of the products. BaSO$_4$ was used as a reflectance standard. A Bruker ECS106 X-band spectrometer was used to characterize the electron spin resonance (ESR) signals of radicals spin-trapped by spintrap reagent 5,5-dimethy-1-pirroline-N-oxide (DMPO) (purchased from Sigma Chemical Co). Electrochemical impedance spectroscopy (EIS) was performed in the frequency range of 10^5− 10^{-2} Hz with the initial potential (0 V) in 0.5 M H$_2$SO$_4$. The photoelectric current (PC) responses measurements were performed using a CHI 660B electrochemical workstation with a standard three-electrode cell at room temperature.

2.4. Photocatalytic Hydrogen Production. The experiment of photocatalytic H$_2$ production was carried out in a Lab-H$_2$ photocatalytic system. A 300 W xenon arc lamp with a optical filter ($\lambda > 420$ nm) was applied as the light source and vertically placed on the top of the reactor. In a typical photocatalytic H$_2$ production experiment, 0.05 g photocatalyst was dispersed with vigorous string in 200 mL of a

20% methanol aqueous solution and stirred continuously to ensure uniform irradiation of the catalyst suspension during the whole experiment. A certain amount of $H_2PtCl_6\cdot6H_2O$ aqueous solution was dripped into the system for loading 0.6% Pt nanoparticles onto the surface of photocatalyst by a photochemical reduction deposition method. Before irradiation, the system was vacuumized to remove the dissolved oxygen in water. During the whole reaction process, the fan in system was kept open to maintain the balance of system gas concentration. A certain amount of generated gas was collected once an hour, and the amout of hydrogen content was analyzed by gas chromatograph (GC-14C, Shimadzu, Japan, TCD, with argon as a carrier gas).

The apparent quantum efficiency (QE) was carried out in a dark room. Four low-power certain wavelength (420 nm) LEDs (4 W) were applied as light sources. The LEDs were positioned 1 cm away from the reactor in four vertical directions. The QE was calculated according to eq 1:

$$QE(\%) = \frac{\text{number of reacted electrons}}{\text{number of incident photons}} \times 100$$

$$QE(\%) = \frac{\text{number of evolved } H_2 \text{ molecules} \times 2}{\text{number of incident photons}} \times 100 \quad (1)$$

3. RESULT AND DISCUSSION

XRD analysis was used to investigate the crystal phase of semiconductor photocatalysts. The XRD patterns of g-C_3N_4, $InVO_4$, and g-C_3N_4/$InVO_4$ composites with different mass fraction of g-C_3N_4 content is shown in Figure 1. The diffraction
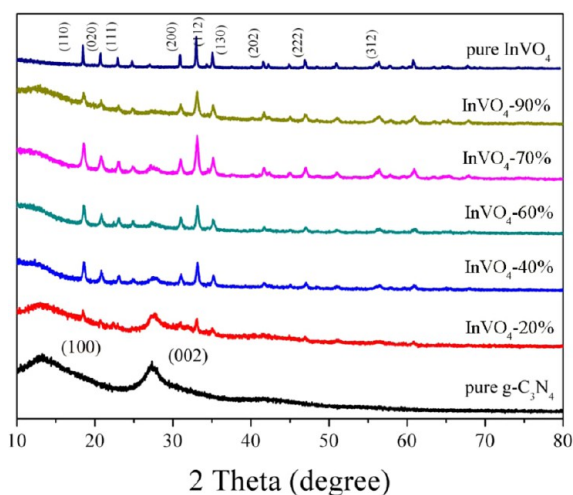

Figure 1. XRD patterns of g-C_3N_4, $InVO_4$, and g-C_3N_4/nano-$InVO_4$ composites with different mass ratios.

peaks of pure $InVO_4$ are well-indexed as an orthorhombic phase of $InVO_4$ and match very well with the standard card (JCPDS 48-0898). The characteristic peaks of pure $InVO_4$ are sharp and strong, which indicate that the reaction time and temperature are suitable for $InVO_4$ well-crystal. The diffraction peaks of pure g-C_3N_4 show that two diffraction peaks at 27.4° and 13.1° can be indexed as (0 0 2) and (1 0 0) diffraction planes,[44,45] respectively. The main characteristic diffraction peaks of g-C_3N_4/$InVO_4$ nanocomposites did not obviously change after hydrothermal reaction, which indicated that the hydrothermal process could not destroy the crystal of g-C_3N_4 sheets.

Figure S1 shows the typical FT-IR spectra of g-C_3N_4/$InVO_4$ composites. As can be seen, the peaks at 1250 cm^{-1}, 1324 cm^{-1},

1420 cm^{-1}, 1573 cm^{-1}, and 1637 cm^{-1} could contribute to the typical stretching modes of CN heterocycles,[46] whereas the peak at 810 cm^{-1} could contribute to the characteristic breathing mode of triazine units in g-C_3N_4.[47] In addition, the typical stretching mode of N−H at 3200 cm^{-1} was also observed. The FT-IR spectrum of pure-$InVO_4$ revealed that peaks at 750, 780, and 910 cm^{-1} are assigned to V−O−In stretching. In the case of g-C_3N_4/$InVO_4$ composites, with the decrease of the g-C_3N_4 mass fraction, the peaks of g-C_3N_4 were weaken and those of $InVO_4$ were strengthen.

The structures of pure g-C_3N_4 are shown in Figure 2(a, b). Figure 2(a) shows that the pure g-C_3N_4 possess layered graphene-like structures, and some porous structures were also found, which could be the result from the released gas (CO_2, H_2O, NH_3) during the thermal decomposition.[48] The surface of g-C_3N_4 sheets were smooth and no nanoparticles were found. High-resolution in Figure 2(b) shows that the thickness of urea-drived g-C_3N_4 sheets ranged from 30 to 70 nm. The structure and morphology of A20 nanocomposites are shown in Figure 2(c, f). Figure 2(c) shows that the $InVO_4$ nanoparticles dispersed on the surface of g-C_3N_4 sheets uniformly. Figure 2(d) shows that both the g-C_3N_4 and $InVO_4$ nanoparticles are in close contact. Figure 2(e, f) shows that $InVO_4$ nanoparticles exhibit spherical-like nanoparticles with an average diameter of approximately 20−30 nm, which were well dispersed onto the surface of g-C_3N_4 to form a heterojunction. The interface between g-C_3N_4 and $InVO_4$ nanoparticles were also found.

The HR-TEM images of pure g-C_3N_4, A30 and A20 sample are also shown in Figure 3. The structure of g-C_3N_4 sheets are clearly seen in Figure 3(a, b). The calculated d value of 0.315 nm corresponds to the (0 0 2) crystallographic plane of g-C_3N_4.[49] Figure 3(c) reveals that the $InVO_4$ nanoparticles dispersed onto the surface of g-C_3N_4. The HRTEM in Figure 3(d) showed that the $InVO_4$ nanoparticles displayed aggregation with unsatisfactory dispersity, which was attributed to the increasing of $InVO_4$ mass fraction. Figure 3(e,f) exhibits that g-C_3N_4 and $InVO_4$ were close enough to form an intimate interface. The size of $InVO_4$ nanoparticles was appropriate 20 nm and interplanar spacing values of 0.344 nm correspond to the d values of the (2 2 0) planes for $InVO_4$.[50]

For investigating the formation process of g-C_3N_4/$InVO_4$ nanojunction, a series of products with different mass fraction of g-C_3N_4 were obtained. As can be seen in Figure 4(a), the surface of original g-C_3N_4 was smooth without any nanoparticles. A20 is shown in Figure 4(b) and it can be seen that most of the g-C_3N_4 surface is effectively covered with appropriate $InVO_4$ nanoparticles, as was the interfacial contact between g-C_3N_4 and $InVO_4$. In addition, the density of $InVO_4$ nanoparticles deposited on the g-C_3N_4 surface became more and more intensive with the increase of $InVO_4$ mass fraction. In the case of A40 sample, the surface of g-C_3N_4 was completely covered by $InVO_4$ nanoparticles and tended to organize into microscale aggregates, which is shown in Figure 4(c). However, further increasing of $InVO_4$ mass fraction caused more aggregation, which more $InVO_4$ microspheres emerged. As shown in Figure 4(d), most of the $InVO_4$ nanoparticles assembled microscale aggregates spontaneously, and the remaining $InVO_4$ nanoparticles covered the surface of g-C_3N_4 sheets at the same time. When the mass ratio of $InVO_4$ content reached 80%, the $InVO_4$ microspheres become the main morphology of $InVO_4$ content. The dispersed g-C_3N_4 sheets owed to the crystal growth of $InVO_4$ between the interlayers of g-C_3N_4 sheets during the hydrothermal reaction, which caused

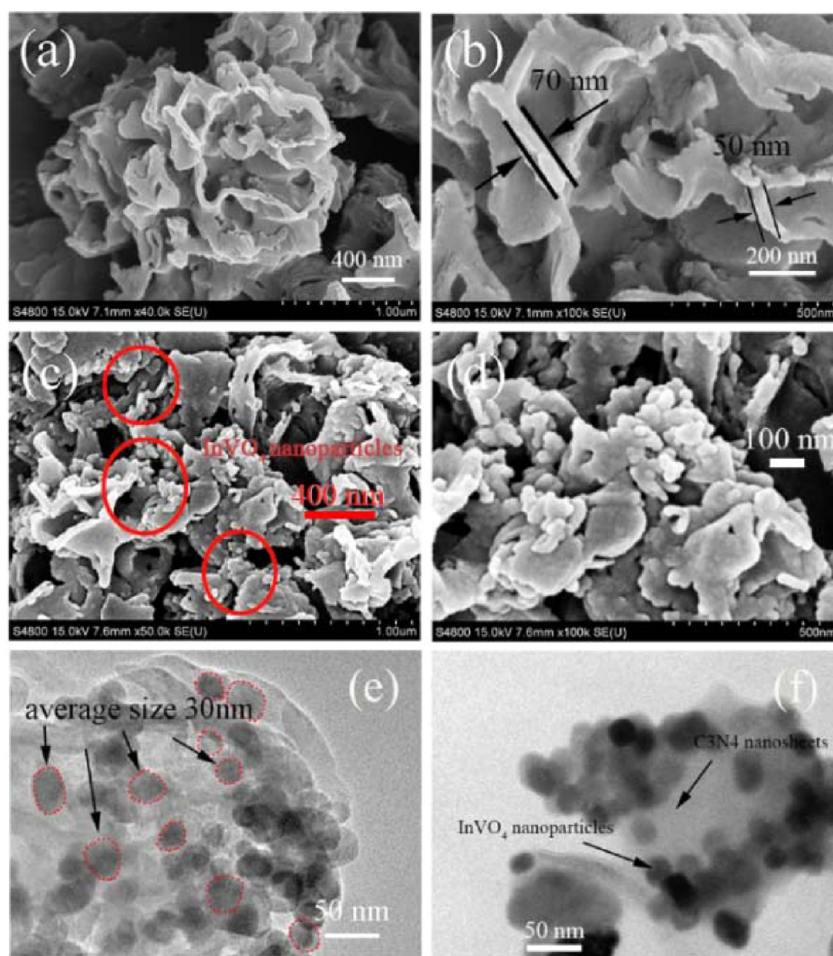**Figure 2.** (a) SEM images of g-C_3N_4, (b) High-magnification SEM of g-C_3N_4, (c, d) SEM and High-magnification SEM images of g-$C3N_4$/$InVO_4$ composites with a mass ratio of 80:20, (e, f) TEM images of g-C_3N_4/$InVO_4$ composites with a mass ratio of 80:20.

the exfoliation of the g-C_3N_4 sheets.[51,52] Figure 4(f) shows the $InVO_4$ microspheres with the diameter of 2−3 μm consisted of nanoparticle self-assembly. To further investigate the effects of g-C_3N_4 mass fraction on the structure of composites, TEM images of A5, A30, A40, A80 are presented in Figure 5. Little nanoparticles are shown in Figure 5(a). Figure 5(b) reveals that the $InVO_4$ nanoparticles were uniformly dispersed on the surface of g-C_3N_4 sheets. The $InVO_4$ nanoparticles and microscale aggregates appear in Figure 5(c) at the same time. Figure 5(d) showed that the g-C_3N_4 sheets contacted with the $InVO_4$ microspheres tightly.

Based on Figures 4 and 5, a possible formation mechanism of g-C_3N_4/$InVO_4$ composites is described in Scheme 2. Obviously, the structure of $InVO_4$ ranged from microspheres (2 μm) to nanoparticles (20 nm) with the increasing of g-C_3N_4 mass fraction, which strongly confirmed that the g-C_3N_4 sheets played vital role in the formation of the nanojunction. Many investigations showed that large specific surface area and two-dimensional structure of g-C_3N_4 could provide a large scaffold for anchoring various substrates.[26,27] In addition, the surface of urea-derievd graphitic g-C_3N_4 possessed positive charge with abundant alamino groups (C-NHx),[53] which could provide a suitable environment for attracting negative charge particles via electrostatic attraction.[54] Accordingly, in our study, the VO_3^{3-} ions could adsorb onto g-C_3N_4 sheets via the electrostatic force in g-C_3N_4 suspension. The anchored VO^{3-} ions would form $InVO_4$ nanocrystals in situ on the surface of g-C_3N_4 sheets

during the hydrothermal reaction, then the tiny nanocrystal nucleus grows into the nanoparticles through oriented growth on the surface of g-C_3N_4 support during the hydrothermal reaction.[55] Eventually, the $InVO_4$ nanoparticles uniformly and tightly distribute onto the surface of g-C_3N_4 sheets (process 1). However, with the increase of $InVO_4$ mass ratio, the capacity of electrostatic attraction between g-C_3N_4 and VO_3^{3-} ions was decreased because the effective positive charge surface of g-C_3N_4 was decreasing. When the mass fraction of $InVO_4$ was more than 30%, the excess of VO_3^{3-} ions could not tightly adsorb on the surface of g-C_3N_4 sheets and would grow into $InVO_4$ nanoparticles freely during the hydrothermal reaction. However, these free $InVO_4$ nanocrystals possessed high specific surface energy, which would assemble spontaneously and form hierarchical microspheres for reducing the interfacial energy.[56,57] As a result, part of $InVO_4$ nanoparticles uniformly grew on the surface of g-C_3N_4 due to the strong electrostatic attraction between VO_3^{3-} ions and C-NH$_x$, whereas other $InVO_4$ nanoparticles were densely self-assembled and formed 3D hierarchical structures which covered the g-C_3N_4 sheets (process 2). With the mass fraction of free $InVO_4$ nanoparticles further increasing, the crystal growth of nanoparticles would cause the exfoliation of the g-C_3N_4 sheets.[51,52] The $InVO_4$ microspheres could directly contacted with g-C_3N_4 sheets, which were shown in Figure 3(d−e) and Figure 4(d), respectively (process 3). The pure $InVO_4$ 3D hierarchical structures was obtained without introducing any g-C_3N_4. It

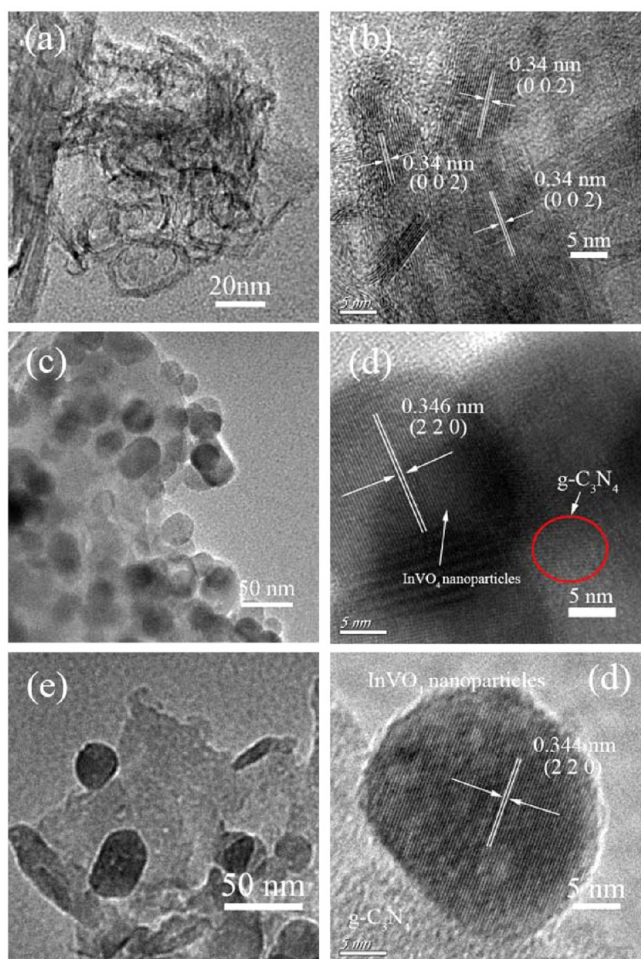**Figure 3.** TEM and HRTEM of pure g-C$_3$N$_4$ (a, b), g-C$_3$N$_4$/InVO$_4$ composites with a mass of 70:30 (c, d), g-C$_3$N$_4$/InVO$_4$ composites with a mass of 80:20 (e, f).

Figure 4. SEM images of different InVO$_4$ mass ratio of g-C$_3$N$_4$/InVO$_4$ composites: (a) 0%, (b) 20%, (c) 40%, (d) 60%, (e) 80%, (f) pure InVO$_4$.

reveals that when the particles of InVO$_4$ nanoparticles were not restricted by the functional alamino groups on the surface of g-C$_3$N$_4$ sheets, they would assemble spontaneously in a random way to form 3D microspheres (process 4).[58] All in all, the results clearly confirmed that the mass ratio of g-C$_3$N$_4$ could be a key parameter for formation of g-C$_3$N$_4$/InVO$_4$ nanocomposites. The positive charge and 2D structure of g-C$_3$N$_4$ sheets can provide a suitable environment for the growth of nanoparticles, which we propose as a novel method to synthesize monodispersed nanojunctions.

The optical property of g-C$_3$N$_4$/InVO$_4$ composites was characterized using UV−vis diffuse reflectance spectroscopy. As shown in Figure 6(a), g-C$_3$N$_4$ holds an absorption edge of 430 nm. A80 show significant light absorption beyond 450 nm which is consistent with the InVO$_4$ microspheres.[58] However, A20 and A30 samples possess blue-shifted absorption edge compared with pure g-C$_3$N$_4$, which indicated that the band gap of photocatalysts enlarged.[32,33]

Figure S2 shows the size and structure of InVO$_4$ microspheres and InVO$_4$ nanoparticles. As can be seen, the size of InVO$_4$ microspheres was about 2 μm, whereas the size of InVO$_4$ nanoparticles was only 20 nm. To confirm the enlarged band gap was due to the size change of InVO$_4$,[42] see the UV−vis spectra of InVO$_4$ nanoparticles, and InVO$_4$ microspheres in Figure 6(b). As can be seen, the absorption edge of InVO$_4$
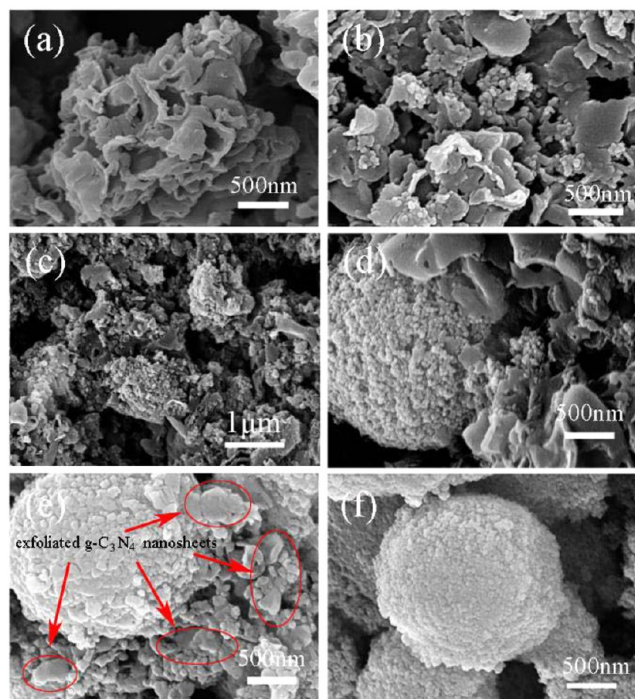
nanoparticles was significantly much lower than InVO$_4$ microspheres and the band gap energy of the InVO$_4$ nanoparticles (3.1 eV) is much larger than that of InVO$_4$ microspheres (2.4 eV). Therefore, the InVO$_4$ nanoparticles with large band gap (3.1 eV) could enlarge the band gap of g-C$_3$N$_4$/InVO$_4$ nanocomposites, which caused the blue-shifted absorption edge. A80 sample show significant absorption range from 425 to 500 nm, which confirmed that InVO$_4$ microspheres were existed.

The energy band positions of conduction band (CB) and valence band (VB) of InVO$_4$ nanoparticles and InVO$_4$ microspheres can be calculated with the following equation:

$$E_{CB} = X - E_e - 0.5E_g \tag{2}$$

$$E_{VB} = E_{CB} + E_g \tag{3}$$

where E_{CB} is the CB edge potential, X is the electronegativity of the semiconductor, which is the geometric mean of the electronegativity of the constituent atoms, E_e is the energy of free electrons on the hydrogen scale (4.5 eV), and E_g is the bandgap energy of the semiconductor.

The CB potentials of InVO$_4$ nanoparticles and InVO$_4$ microspheres have been calculated to be −0.33 and 0.02 eV, respectively. Therefore, the energy of photogenerated electronics for g-C$_3$N$_4$/micro-InVO$_4$ and g-C$_3$N$_4$/nano-InVO$_4$ have quite a different after charge transfer because of different CB potentials of InVO$_4$ nanoparticles and InVO$_4$ microspheres. The InVO$_4$ nanoparticles possessed much higher CB potentials than InVO$_4$ microspheres which caused the redox ability of g-C$_3$N$_4$/nano-InVO$_4$ was much stronger than g-C$_3$N$_4$/micro-InVO$_4$.

In order to further confirm the above conclusion, ESR experiments were carried out. Figure 7 showed ESR spectra measured as the effect of light irradiation on the bare g-C$_3$N$_4$,

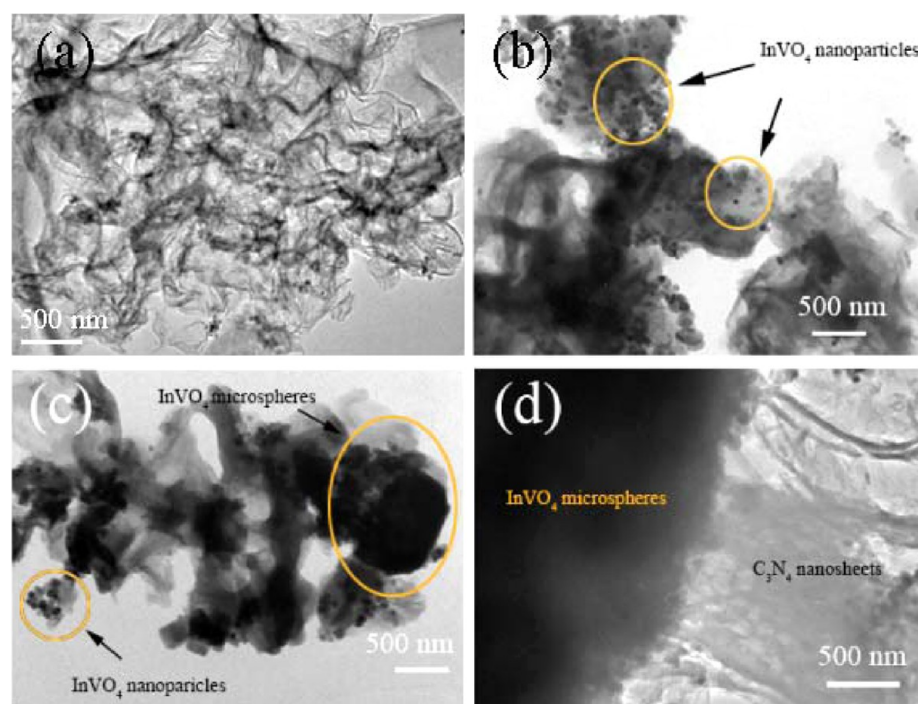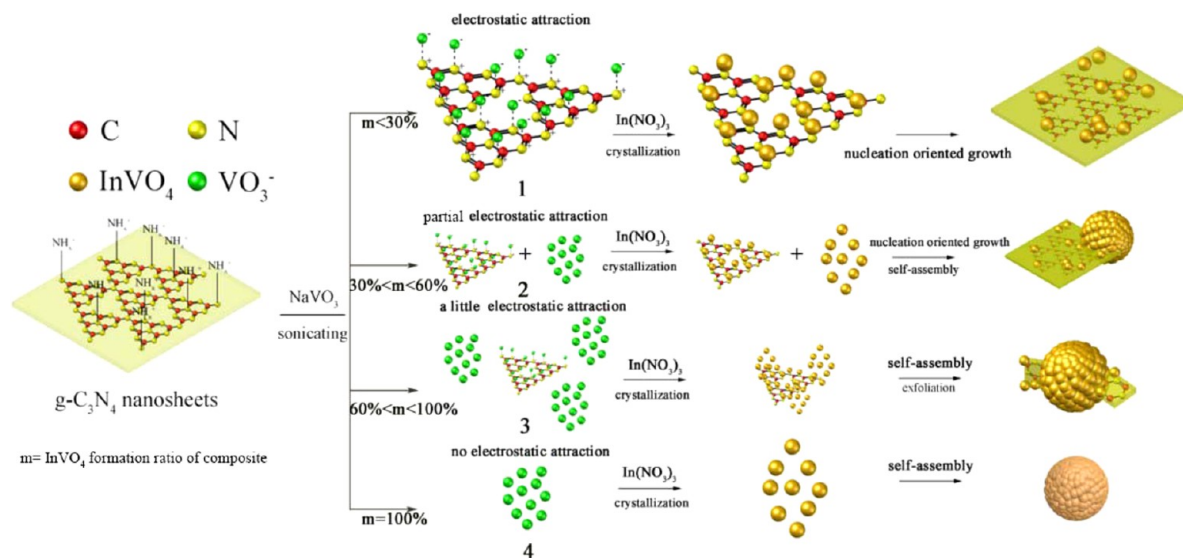**Figure 5.** TEM images of different InVO$_4$ content of g-C$_3$N$_4$/InVO$_4$ composites (a) 5%, (b) 20%, (c) 40%, (d) 80%.

Scheme 2. Possible Formation Mechanism of g-C$_3$N$_4$/InVO$_4$ Composites with Different Mass Ratio of InVO$_4$

A20 and A40 photocatalysts at room temperature. The result revealed that the intensity of the characteristic peaks of superoxide radicals for the A20 sample is higher than that of g-C$_3$N$_4$ and A40 sample, which indicated that the A20 sample achieved higher redox ability than pure g-C$_3$N$_4$ and A40 sample. The weaker redox ability of pure g-C$_3$N$_4$ is attributed to the less effective photogenerated electron during light irradiation due to high recombination of photogenerated electron−hole pairs, whereas the weak redox ability of A40 sample is attributed to the lower CB of InVO$_4$ microspheres (0.02 eV) compared with InVO$_4$ nanoparticles (−0.33 eV). The photogenarated electrons in the CB of InVO$_4$ microspheres (0.02 eV) cannot reduce O$_2$ into •O$_2^-$ with the redox potential of −0.046 eV vs. NHE, which would significantly reduced the redox ability.

To verify the heterojunction composed of g-C$_3$N$_4$ sheets and InVO$_4$ nanoparticles could promote the charge transfer and inhibit the recombination of charge-pairs, a series of experiments, such as electrochemical impedance spectroscopy (EIS), photoelectrochemical measurements, and photoluminescence (PL) emission spectra were performed. Figure 8(a) shows the typical EIS curve for pure g-C$_3$N$_4$ photoanode and g-C$_3$N$_4$/InVO$_4$ nanocompsites photoanode in 0.5 M H$_2$SO$_4$ under illumination. A smaller diameter was found in the curve of A20 photoanode compared to bare g-C$_3$N$_4$, which indicated the resistance between A20/electrolyte interface was much smaller than g-C$_3$N$_4$/electrolyte. The result revealed that the nanojunction between g-C$_3$N$_4$ and InVO$_4$ nanoparticles would obviously improve the rate of charge transfer. However, the diameter of A40 was larger than A20, which revealed that the
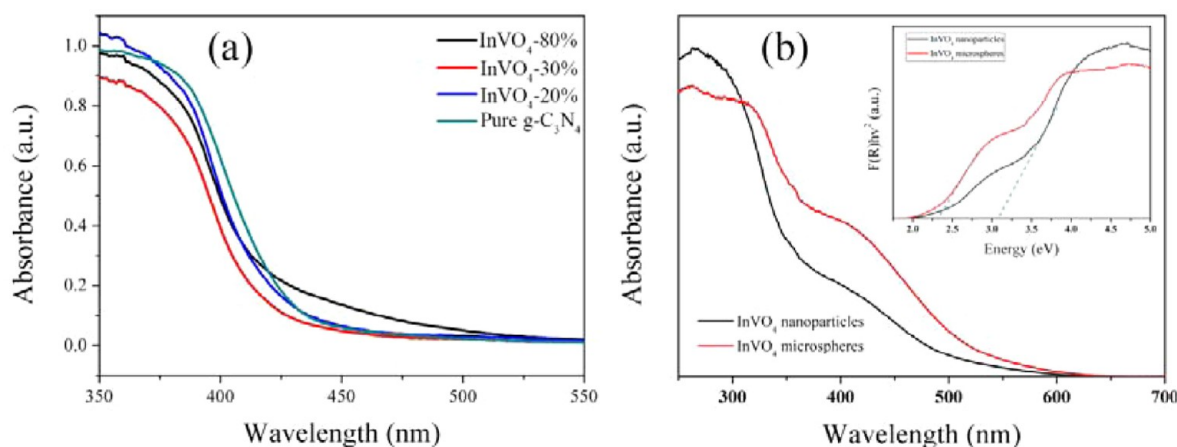
Figure 6. UV–vis spectra of (a) g-C$_3$N$_4$/InVO$_4$ composites; (b) InVO$_4$ nanoparticles and InVO$_4$ microspheres with the corresponding calculated band gap energy of different samples (inset).
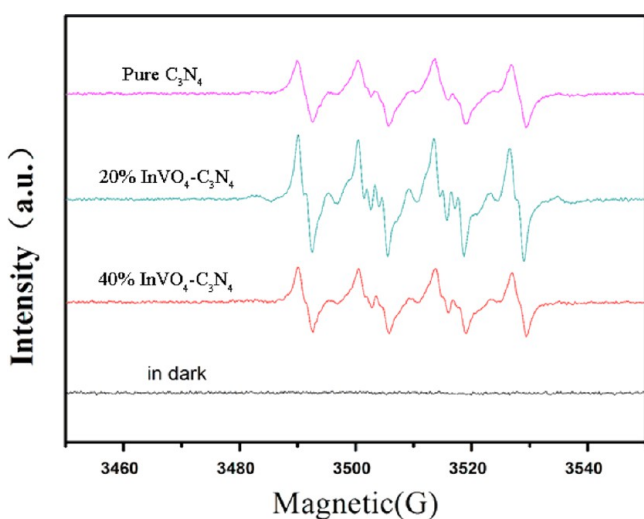

Figure 7. ESR signals of the DMPO-•O$_2^-$ with irradiation for 20 s in methanol dispersion.

resistance of A20 was smaller than A40. As shown in Figure 4 and Figure 5, the increasing resistance of A40 sample could be contributed that the InVO$_4$ nanoparticles were too densely covered on the surface of g-C$_3$N$_4$, which reduced the effective area of light absorption for g-C$_3$N$_4$ sheets. The transient

photocurrent responses of bare g-C$_3$N$_4$, A20 and A40 samples were recorded for three on-off cycles under visible-light irradiation and are revealed in Figure 8(d). The A20 sample show the highest photocurrent intensity of the three samples, whereas A40 and pure g-C$_3$N$_4$ have the middle and lowest values, respectively. Therefore, the A20 and A40 samples achieved more effective separation of charge-hole pairs than bare g-C$_3$N$_4$, which is consistent with the EIS measurements. The reduced photocurrent intensity of A40 was contributed to the decreasing effective area of light absorption for g-C$_3$N$_4$ sheets. Figure S3 presents the PL spectra of pure g-C$_3$N$_4$, A20 with an excitation wavelength of 320 nm. The g-C$_3$N$_4$ sheets possess an obvious emission peak at about 435 nm, which corresponds to the band gap of g-C$_3$N$_4$. The InVO$_4$ nanopaticles were dispersed on the surface of g-C$_3$N$_4$ tightly, which formed outstanding interface to improve the rate of charge transfer and inhibit the recombination of charge-hole pairs. The PL emission intensity of g-C$_3$N$_4$/InVO$_4$ composites got an obvious decrease compared with bare g-C$_3$N$_4$, which suggests that the charge recombination of g-C$_3$N$_4$ can be efficiently prevented.[59]

3.5. Photocatalytic Activity and Photostability. To investigate the performance of prepared catalysts, we carried out hydrogen evolution experiments in 20% methyl alcohol solution with 0.6% Pt as a cocatalyst. Figure 9(a) shows the time courses of H$_2$ evolution of different g-C$_3$N$_4$/InVO$_4$

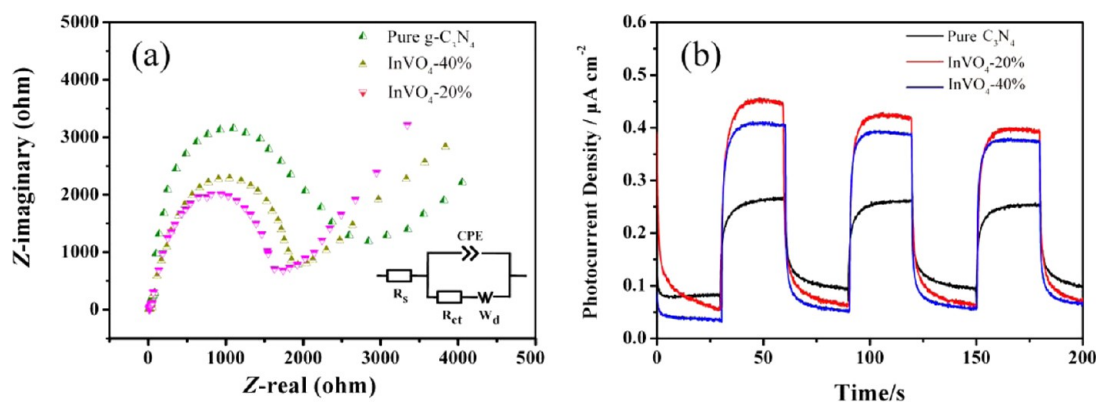**Figure 8.** (a) EIS obtained for pure C$_3$N$_4$ and g-C$_3$N$_4$/InVO$_4$ composites under light irradiation in 0.5 M H$_2$SO$_4$ aqueous solution, (b) Transient photocurrent responses of pure C$_3$N$_4$ and g-C$_3$N$_4$/InVO$_4$ composites collected in 1.0 M NaOH electrolyte.
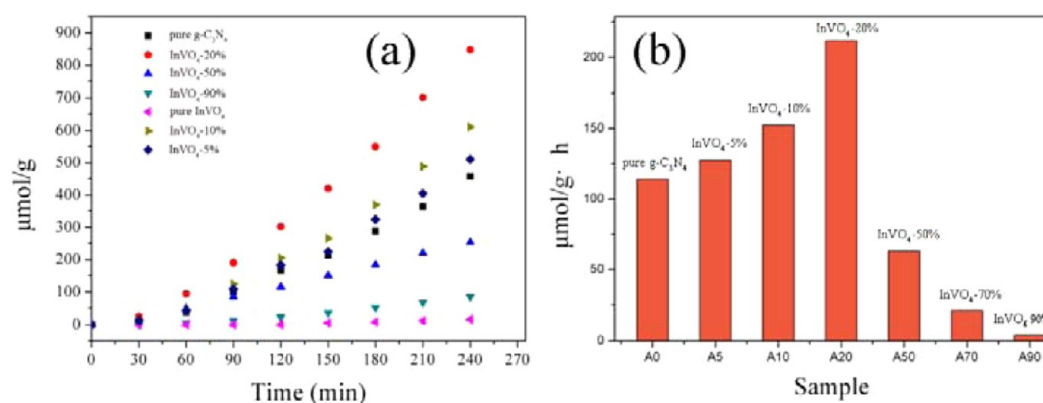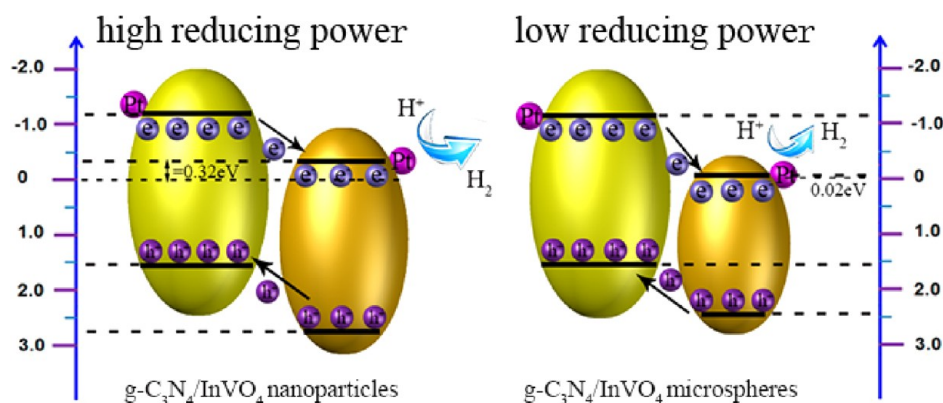
Figure 9. (a) Plots of photocatalytic H_2 evolution amount visible light irradiation ($\lambda > 420$ nm) time for different samples, (b) Comparison of the visible light induced H_2 evolution rate for different samples.

Scheme 3. Schematic Illustration of g-C$_3$N$_4$/InVO$_4$ Composites under Visible Light Irradiation

composites. It is clear that A5, A10, A20 showed significantly enhanced photocatalytic activity as compared with pure g-C$_3$N$_4$ and pure InVO$_4$. A20 showed highest photocatalyst activity of H$_2$ production with the rate of 212 μmol/g·h. The apparent quantum efficiency (QE) of A20 was 4.9% at 420 nm. To examine the stability of the obtained g-C$_3$N$_4$/InVO$_4$ nanocomposites, recycling rest was performed on the hydrogen production activity of A20 sample after 5 h. Figure S4 showed no obvious decrease of H$_2$ production rate between 5 and 20 h, indicating the obtained g-C$_3$N$_4$/InVO$_4$ nanocomposites showed photostability during reaction time.

The photocatalytic mechanism would be clarified in detail. A photocatalytic mechanism for enhanced photocatalytic activity of g-C$_3$N$_4$/InVO$_4$ nanojunction was proposed in Scheme 3. First, the enhanced H$_2$ production was due to the improved charge transfer through the interface between InVO$_4$ nanoparticles and g-C$_3$N$_4$ sheets, which significantly inhibited the recombination of photogenerated electron−hole pairs. When the g-C$_3$N$_4$/InVO$_4$ nanojunction was irradiated by visible light, photogenerated electrons are promoted from the valence bands (VB) of g-C$_3$N$_4$ and InVO$_4$ to their conduction bands (CB), respectively. Because of the band gap discontinuity, the photogenerated electrons on the CB of g-C$_3$N$_4$ can be transferred to the CB of InVO$_4$ and reduced hydrogen ions in water into hydrogen, which obviously inhibited the recombination of photogenerated electron−hole pairs. Second, the reducing power of g-C$_3$N$_4$/nano-InVO$_4$ nanocomposites was much stronger than that of g-C$_3$N$_4$/micro-InVO$_4$ composites due to the different energy band of InVO$_4$ nanoparticles and InVO$_4$ microspheres, which was demon-

strated by ESR data. Therefore, the g-C$_3$N$_4$/InVO$_4$ nanocomposites could not only improve the charge-separation efficiency but also achieve a strong driving force for H$_2$ production compared with bare g-C$_3$N$_4$ and g-C$_3$N$_4$/micro-InVO$_4$ composites, respectively. Owing to the above reasons, the photocatalytic activity of g-C$_3$N$_4$/nano-InVO$_4$ nanojunction was much higher than that of bare g-C$_3$N$_4$ and g-C$_3$N$_4$/micro-InVO$_4$ composites.

4. CONCLUSION

g-C$_3$N$_4$/InVO$_4$ nanocomposites were prepared by in situ growth InVO$_4$ nanoparticles onto surface of g-C$_3$N$_4$ sheets via hydrothermal process. The g-C$_3$N$_4$ sheets played vital role in the formation of g-C$_3$N$_4$/InVO$_4$ nanocomposites, which revealed that g-C$_3$N$_4$ is a promising support for in situ growth of nanosize materials. The formation of interfaces could promote the charge transfer and inhibited recombination of charge-hole pairs, which significantly improved the photocatalytic activity of H$_2$ evolution from water-splitting. The A20 sample with desired interfaces and structures exhibited best photocatalytic H$_2$ evolution of 212 μmol/g·h. This study provides a novel visible-light-reponse heterojunction-type photocatalytic systems based on g-C$_3$N$_4$ and multiple metal oxide.

■ ASSOCIATED CONTENT

S **Supporting Information**

The Supporting Information is available free of charge on the ACS Publications website at DOI: 10.1021/acsami.5b05715.

Figures S1−S4 (PDF)

■ AUTHOR INFORMATION

Corresponding Author
*E-mail: swd1978@ujs.edu.cn. Tel. +86 511 8879 0187. Fax: +86 511 8879 1108.

Notes
The authors declare no competing financial interest.

■ REFERENCES

(1) Yun, H. J.; Lee, H.; Kim, N. D.; Lee, D. M.; Yu, S.; Yi, J. A Combination of Two Visible-Light Responsive Photocatalysts for Achieving the Z-Scheme in the Solid State. *ACS Nano* **2011**, *5*, 4084−4090.

(2) Iwashina, K.; Iwase, A.; Ng, Y. H.; Amal, R.; Kudo, A. Z-Schematic Water Splitting into H_2 and O_2 Using Metal Sulfide as a Hydrogen-Evolving Photocatalyst and Reduced Graphene Oxide as a Solid-State Electron Mediator. *J. Am. Chem. Soc.* **2015**, *137*, 604−607.

(3) Iwashina, K.; Kudo, A. Rh-Doped $SrTiO_3$ Photocatalyst Electrode Showing Cathodic Photocurrent for Water Splitting under Visible-Light Irradiation. *J. Am. Chem. Soc.* **2011**, *133*, 13272−13275.

(4) Liu, G.; Niu, P.; Yin, L.; Cheng, H.-M. α-Sulfur Crystals as A Visible-Light-Active Photocatalyst. *J. Am. Chem. Soc.* **2012**, *134*, 9070−9073.

(5) Zhu, J.; Zäch, M. Nanostructured Materials for Photocatalytic Hydrogen Production. *Curr. Opin. Colloid Interface Sci.* **2009**, *14*, 260−269.

(6) Chen, X.; Shen, S.; Guo, L.; Mao, S. S. Semiconductor-based Photocatalytic Hydrogen Generation. *Chem. Rev.* **2010**, *110*, 6503−6570.

(7) Kudo, A.; Miseki, Y. Heterogeneous Photocatalyst Materials for Water Splitting. *Chem. Soc. Rev.* **2009**, *38*, 253−278.

(8) Li, K.; Chai, B.; Peng, T.; Mao, J.; Zan, L. Preparation of $AgIn_5S_8/TiO_2$ Heterojunction Nanocomposite and Its Enhanced Photocatalytic H_2 Production Property under Visible Light. *ACS Catal.* **2013**, *3*, 170−177.

(9) Tian, Y.; Chang, B.; Lu, J.; Fu, J.; Xi, F.; Dong, X. Hydrothermal Synthesis of Graphitic Carbon Nitride-Bi_2WO_6 Heterojunctions with Enhanced Visible Light Photocatalytic Activities. *ACS Appl. Mater. Interfaces* **2013**, *5*, 7079−7085.

(10) Fan, H.; Li, H.; Liu, B.; Lu, Y.; Xie, T.; Wang, D. Photoinduced Charge Transfer Properties and Photocatalytic Activity in $Bi_2O_3/BaTiO_3$ Composite Photocatalyst. *ACS Appl. Mater. Interfaces* **2012**, *4*, 4853−4857.

(11) Hou, Y.; Zuo, F.; Dagg, A.; Feng, P. Visible Light-Driven α-Fe_2O_3 Nanorod/Graphene/$BiV_{1-x}Mo_xO_4$ Core/Shell Heterojunction Array for Efficient Photoelectrochemical Water Splitting. *Nano Lett.* **2012**, *12*, 6464−6473.

(12) Zhou, P.; Yu, J.; Jaroniec, M. All-Solid-State Z-scheme Photocatalytic Systems. *Adv. Mater.* **2014**, *26*, 4920−4935.

(13) Wang, X.; Maeda, K.; Thomas, A.; Takanabe, K.; Xin, G.; Carlsson, J. M.; Domen, K.; Antonietti, M. A Metal-free Polymeric Photocatalyst for Hydrogen Production from Water under Visible Light. *Nat. Mater.* **2009**, *8*, 76−80.

(14) Zhao, Z.; Sun, Y.; Dong, F. Graphitic Carbon Nitride Based Nanocomposites: A Review. *Nanoscale* **2015**, *7*, 15−37.

(15) Cao, S.; Yu, J. g-C_3N_4-Based Photocatalysts for Hydrogen Generation. *J. Phys. Chem. Lett.* **2014**, *5*, 2101−2107.

(16) Zhang, J.; Yu, J.; Jaroniec, M.; Gong, J. R. Noble Metal-Free Reduced Graphene Oxide-$Zn_xCd_{1-x}S$ Nanocomposite with Enhanced Solar Photocatalytic H_2-Production Performance. *Nano Lett.* **2012**, *12*, 4584−4589.

(17) Chen, J.; Shen, S.; Guo, P.; Wang, M.; Wu, P.; Wang, X.; Guo, L. In-Situ Reduction Synthesis of Nano-Sized Cu_2O Particles Modifying g-C_3N_4 for Enhanced Photocatalytic Hydrogen Production. *Appl. Catal., B* **2014**, *152−153*, 335−341.

(18) Li, Z.; Wang, J.; Zhu, K.; Ma, F.; Meng, A. Ag/g-C_3N_4 Composite Nanosheets: Synthesis and Enhanced Visible Photocatalytic Activities. *Mater. Lett.* **2015**, *145*, 167−170.

(19) Yang, Z.; Li, J.; Cheng, F.; Chen, Z.; Dong, X. BiOBr/Protonated Graphitic C_3N_4 Heterojunctions: Intimate Interfaces by Electrostatic Interaction and Enhanced Photocatalytic Activity. *J. Alloys Compd.* **2015**, *634*, 215−222.

(20) He, Y.; Wang, Y.; Zhang, L.; Teng, B.; Fan, M. High-Efficiency Conversion of CO_2 to Fuel over ZnO/g-C_3N_4 Photocatalyst. *Appl. Catal., B* **2015**, *168−169*, 1−8.

(21) Zhao, W.; Guo, Y.; Wang, S.; He, H.; Sun, C.; Yang, S. A Novel Ternary Plasmonic Photocatalyst: Ultrathin g-C_3N_4 Nanosheet Hybrided by $Ag/AgVO_3$ Nanoribbons with Enhanced Visible-Light Photocatalytic Performance. *Appl. Catal., B* **2015**, *165*, 335−343.

(22) Zhu, T.; Song, Y.; Ji, H.; Xu, Y.; Song, Y.; Xia, J.; Yin, S.; Li, Y.; Xu, H.; Zhang, Q.; Li, H. Synthesis of g-C_3N_4/Ag_3VO_4 Composites with Enhanced Photocatalytic Activity under Visible Light Irradiation. *Chem. Eng. J.* **2015**, *271*, 96−105.

(23) Cai, Q.; Shen, J.; Feng, Y.; Shen, Q.; Yang, H. Template-free Preparation and Characterization of Nanoporous g-C_3N_4 with Enhanced Visible Photocatalytic Activity. *J. Alloys Compd.* **2015**, *628*, 372−378.

(24) Chen, J.; Hong, Z.; Chen, Y.; Lin, B.; Gao, B. One-Step Synthesis of Sulfur-doped and Nitrogen-deficient g-C_3N_4 Photocatalyst for Enhanced Hydrogen Evolution under Visible Light. *Mater. Lett.* **2015**, *145*, 129−132.

(25) Li, W.; Feng, C.; Dai, S.; Yue, J.; Hua, F.; Hou, H. Fabrication of Sulfur-Doped g-C_3N_4/Au/CdS Z-Scheme Photocatalyst to Improve the Photocatalytic Performance under Visible Light. *Appl. Catal., B* **2015**, *168−169*, 465−471.

(26) Sun, L.; Zhao, X.; Jia, C.-J.; Zhou, Y.; Cheng, X.; Li, P.; Liu, L.; Fan, W. Enhanced Visible-Light Photocatalytic Activity of g-C_3N_4−$ZnWO_4$ by Fabricating A Heterojunction: Investigation Based on Experimental and Theoretical Studies. *J. Mater. Chem.* **2012**, *22*, 23428−23438.

(27) Li, H.; Liu, J.; Hou, W.; Du, N.; Zhang, R.; Tao, X. Synthesis and Characterization of g-C_3N_4/Bi_2MoO_6 Heterojunctions with Enhanced Visible Light Photocatalytic Activity. *Appl. Catal., B* **2014**, *160−161*, 89−97.

(28) Yan, H.; Yang, H. TiO_2−g-C_3N_4 Composite Materials for Photocatalytic H_2 Evolution under Visible Light Irradiation. *J. Alloys Compd.* **2011**, *509*, L26−L29.

(29) Obregón, S.; Colón, G. Improved H_2 Production of Pt-TiO_2/g-C_3N_4-MnO_x Composites by An Efficient Handling of Photogenerated Charge Pairs. *Appl. Catal., B* **2014**, *144*, 775−782.

(30) Wang, J.; Huang, J.; Xie, H.; Qu, A. Synthesis of g-C_3N_4/TiO_2 with Enhanced Photocatalytic Activity for H_2 Evolution by A Simple Method. *Int. J. Hydrogen Energy* **2014**, *39*, 6354−6363.

(31) Shi, F.; Chen, L.; Xing, C.; Jiang, D.; Li, D.; Chen, M. ZnS Microsphere/g-C_3N_4 Nanocomposite Photo-Catalyst with Greatly Enhanced Visible Light Performance for Hydrogen Evolution: Synthesis and Synergistic Mechanism Study. *RSC Adv.* **2014**, *4*, 62223−62229.

(32) Cao, S.-W.; Yuan, Y.-P.; Fang, J.; Shahjamali, M. M.; Boey, F. Y. C.; Barber, J.; Joachim Loo, S. C.; Xue, C. In-Situ Growth of CdS Quantum Dots on g-C_3N_4 Nanosheets for Highly Efficient Photo-

catalytic Hydrogen Generation under Visible Light Irradiation. *Int. J. Hydrogen Energy* **2013**, *38*, 1258−1266.

(33) Zhang, J.; Wang, Y.; Jin, J.; Zhang, J.; Lin, Z.; Huang, F.; Yu, J. Efficient Visible-Light Photocatalytic Hydrogen Evolution and Enhanced Photostability of Core/Shell CdS/g-C$_3$N$_4$ Nanowires. *ACS Appl. Mater. Interfaces* **2013**, *5*, 10317−10324.

(34) Tian, Y.; Ge, L.; Wang, K.; Chai, Y. Synthesis of Novel MoS$_2$/g-C$_3$N$_4$ Heterojunction Photocatalysts with Enhanced Hydrogen Evolution Activity. *Mater. Charact.* **2014**, *87*, 70−73.

(35) Abe, R. Recent Progress on Photocatalytic and Photo-electrochemical Water Splitting under Visible Light Irradiation. *J. Photochem. Photobiol., C* **2010**, *11*, 179−209.

(36) Kang, H. W.; Lim, S. N.; Song, D.; Park, S. B. Organic-inorganic Composite of g-C$_3$N$_4$−SrTiO$_3$:Rh Photocatalyst for Improved H$_2$ Evolution under Visible Light Irradiation. *Int. J. Hydrogen Energy* **2012**, *37*, 11602−11610.

(37) Chen, J.; Shen, S.; Guo, P.; Wu, P.; Guo, L. Spatial Engineering of Photo-active Sites on g-C$_3$N$_4$ for Efficient Solar Hydrogen Generation. *J. Mater. Chem. A* **2014**, *2*, 4605−4612.

(38) Yan, Y.; Liu, X.; Fan, W.; Lv, P.; Shi, W. InVO$_4$ Microspheres: Preparation, Characterization and Visible-Light-Driven Photocatalytic Activities. *Chem. Eng. J.* **2012**, *200−202*, 310−316.

(39) Ye, J.; Zou, Z.; Oshikiri, M.; Matsushita, A.; Shimoda, M.; Imai, M.; Shishido, T. A Novel Hydrogen-Evolving Photocatalyst InVO$_4$ Active under Visible Light Irradiation. *Chem. Phys. Lett.* **2002**, *356*, 221−226.

(40) Liao, L.; Zhang, Q.; Su, Z.; Zhao, Z.; Wang, Y.; Li, Y.; Lu, X.; Wei, D.; Feng, G.; Yu, Q.; Cai, X.; Zhao, J.; Ren, Z.; Fang, H.; Robles-Hernandez, F.; Baldelli, S.; Bao, J. Efficient Solar Water-Splitting Using A Nanocrystalline CoO Photocatalyst. *Nat. Nanotechnol.* **2013**, *9*, 69−73.

(41) Sun, S.; Wang, W.; Li, D.; Zhang, L.; Jiang, D. Solar Light Driven Pure Water Splitting on Quantum Sized BiVO$_4$ without any Cocatalyst. *ACS Catal.* **2014**, *4*, 3498−3503.

(42) Yan, Y.; Cai, F.; Song, Y.; Shi, W. InVO$_4$ Nanocrystal Photocatalysts: Microwave-Assisted Synthesis and Size-Dependent Activities of Hydrogen Production from Water Splitting under Visible Light. *Chem. Eng. J.* **2013**, *233*, 1−7.

(43) Wang, Y.; Herron, N. Nanometer-Sized Semiconductor Clusters: Materials Synthesis, Quantum Size Effects, and Photo-physical Properties. *J. Phys. Chem.* **1991**, *95*, 525−532.

(44) Lee, S. C.; Lintang, H. O.; Yuliati, L. A Urea Precursor to Synthesize Carbon Nitride with Mesoporosity for Enhanced Activity in the Photocatalytic Removal of Phenol. *Chem. - Asian J.* **2012**, *7*, 2139−2144.

(45) Zhang, Y.; Liu, J.; Wu, G.; Chen, W. Porous Graphitic Carbon Nitride Synthesized Via Direct Polymerization of Urea for Efficient Sunlight-Driven Photocatalytic Hydrogen Production. *Nanoscale* **2012**, *4*, 5300−5303.

(46) Xu, J.; Wang, G.; Fan, J.; Liu, B.; Cao, S.; Yu, J. g-C$_3$N$_4$ Modified TiO$_2$ Nanosheets with Enhanced Photoelectric Conversion Efficiency in Dye-Sensitized Solar Cells. *J. Power Sources* **2015**, *274*, 77−84.

(47) Yu, J.; Wang, S.; Low, J.; Xiao, W. Enhanced Photocatalytic Performance of Direct Z-Scheme g-C$_3$N$_4$-TiO$_2$ Photocatalysts for the Decomposition of Formaldehyde in Air. *Phys. Chem. Chem. Phys.* **2013**, *15*, 16883−16890.

(48) Zhou, X.; Luo, Z.; Tao, P.; Jin, B.; Wu, Z.; Huang, Y. Facile Preparation and Enhanced Photocatalytic H$_2$-Production Activity of Cu(OH)$_2$ Nanospheres Modified Porous g-C$_3$N$_4$. *Mater. Chem. Phys.* **2014**, *143*, 1462−1468.

(49) Yan, T.; Yan, Q.; Wang, X.; Liu, H.; Li, M.; Lu, S.; Xu, W.; Sun, M. Facile Fabrication of Heterostructured g-C$_3$N$_4$/Bi$_2$MoO$_6$ Micro-spheres with Highly Efficient Activity under Visible Light Irradiation. *Dalton Trans.* **2015**, *44*, 1601−1611.

(50) Wang, Y.; Dai, H.; Deng, J.; Liu, Y.; Zhao, Z.; Li, X.; Arandiyan, H. Three-Dimensionally Ordered Macroporous InVO$_4$: Fabrication and Excellent Visible-Light-Driven Photocatalytic Performance for Methylene Blue Degradation. *Chem. Eng. J.* **2013**, *226*, 87−94.

(51) Fu, Y.; Wang, X. Magnetically Separable ZnFe$_2$O$_4$−Graphene Catalyst and its High Photocatalytic Performance under Visible Light Irradiation. *Ind. Eng. Chem. Res.* **2011**, *50*, 7210−7218.

(52) Fu, Y.; Xiong, P.; Chen, H.; Sun, X.; Wang, X. High Photocatalytic Activity of Magnetically Separable Manganese Fer-rite−Graphene Heteroarchitectures. *Ind. Eng. Chem. Res.* **2012**, *51*, 725−731.

(53) Martin, D. J.; Qiu, K.; Shevlin, S. A.; Handoko, A. D.; Chen, X.; Guo, Z.; Tang, J. Highly Efficient Photocatalytic H$_2$ Evolution from Water Using Visible Light and Structure-Controlled Graphitic Carbon Nitride. *Angew. Chem., Int. Ed.* **2014**, *53*, 9240−9245.

(54) Cheng, H.; Long, L.; Shu, D.; Wu, J.; Gong, Y.; He, C.; Kang, Z.; Zou, X. The Supercapacitive Behavior and Excellent Cycle Stability of Graphene/MnO$_2$ Composite Prepared by An Electrostatic Self-Assembly Process. *Int. J. Hydrogen Energy* **2014**, *39*, 16151−16161.

(55) Fu, Y.; Chen, Q.; He, M.; Wan, Y.; Sun, X.; Xia, H.; Wang, X. Copper Ferrite-Graphene Hybrid: A Multifunctional Heteroarchitec-ture for Photocatalysis and Energy Storage. *Ind. Eng. Chem. Res.* **2012**, *51*, 11700−11709.

(56) Li, Y.; Cao, M.; Feng, L. Hydrothermal Synthesis of Mesoporous InVO$_4$ Hierarchical Microspheres and Their Photo-luminescence Properties. *Langmuir* **2009**, *25*, 1705−1712.

(57) Noh, T. H.; Kim, D. W.; Seo, S. W.; Cho, I. S.; Kim, D. H.; Han, H. S.; Hong, K. S. Facile Hydrothermal Synthesis of InVO$_4$ Microspheres and Their Visible-Light Photocatalytic Activities. *Mater. Lett.* **2012**, *72*, 98−100.

(58) Zhang, L.; Fu, H.; Zhang, C.; Zhu, Y. Synthesis, Character-ization, and Photocatalytic Properties of InVO$_4$ Nanoparticles. *J. Solid State Chem.* **2006**, *179*, 804−811.

(59) Hou, Y.; Wen, Z.; Cui, S.; Guo, X.; Chen, J. Constructing 2D Porous Graphitic C$_3$N$_4$ Nanosheets/Nitrogen-Doped Graphene/Layered MoS$_2$ Ternary Nanojunction with Enhanced Photoelectro-chemical Activity. *Adv. Mater.* **2013**, *25*, 6291−6297.